3D EIT image reconstruction with GREIT

[1]**Bartłomiej Grychtol, [2]Beat Müller, [3]Andy Adler**

[1]Fraunhofer Project Group for Automation in Medicine and Biotechnology PAMB, Mannheim, Germany, [2]Swisstom AG, Landquart, Switzerland, [3]Systems and Computer Engineering, Carleton University, Ottawa, Canada

E-mail: `andy.adler@carleton.ca`

Abstract. Most applications of thoracic EIT use a single plane of electrodes on the chest from which a transverse image "slice" is calculated. However, interpretation of EIT images is made difficult by the large region above and below the electrode plane to which EIT is sensitive. Volumetric EIT images using two (or more) electrode planes should help compensate, but are little used currently. The Graz consensus reconstruction algorithm for EIT (GREIT) has become popular in lung EIT. One shortcoming of the original formulation of GREIT is its restriction to reconstruction onto a 2D planar image. We present an extension of the GREIT algorithm to 3D and develop open-source tools to evaluate its performance as a function of the choice of stimulation and measurement pattern. Results show 3D GREIT using two electrode layers has significantly more uniform sensitivity profiles through the chest region. Overall, the advantages of 3D EIT are compelling.

1. Introduction

Electrical Impedance Tomography (EIT) creates images of the distribution of impedance within a body from electrical stimulation and measurement at the body surface. EIT is sensitive to movement and changes in conductivity contrasting fluids and gasses. The most common application of EIT is for imaging of the thorax (Adler *et al* 2012), where the physiology of interest (air and blood flow) involves processes which can be imaged by EIT. The vast majority of EIT studies of thoracic function have used a placement of electrodes in a transverse, or slightly oblique (Vonk Noordegraaf *et al* 1996), plane around the chest. Using these electrodes, EIT measurements are made and a 2D image has been reconstructed, representing a "slice" through the chest.

Such EIT images are clinically useful, especially as a "bedside" approach to monitor ventilated patients. In a prone or supine patient without significant obstructive lung disease, lung aeration and perfusion are understood to redistribute primarily in the gravity direction. Since a 2D EIT image from transverse-plane electrodes can provide this gravity-related information, 2D EIT thorax images can be interpreted as representing most of the key clinical information (Adler *et al* 2012).

Overall, however, a 2D EIT "slice" provides limited information on the thorax. First, in many lung pathologies, lung tissue behaviour is significantly inhomogeneous.

The most common examples are obstructive lung diseases which have large regional variations. Additionally, even if we are only interested in a transverse section, the 2D EIT image does not provide a true slice. Because of the diffusive nature of electrical current propagation, EIT is sensitive to conductivity changes in a region above and below the plane of interest. For interpretation of EIT images, it is important to understand the spatial extent of EIT sensitivity. For example, in some cases, the compression of abdominal gas has been indicated as a source of EIT lung image artefacts (Ambrisko *et al* 2015). The extent to which out of plane contributions are shown in the EIT image is determined by the vertical sensitivity profile (Rabbani and Kabir, 1991). The EIT sensitivity region has been described as a "lens shaped" region extending to $\frac{1}{2}$ of the body diameter above and below the electrode plane (Putensen *et al* 2006, Adler *et al* 2015).

Image reconstruction in EIT must solve the ill-conditioning caused by the large differences in sensitivity between internal and near-surface conductivity changes. Several authors have considered 3D EIT reconstruction. Metherall *et al* (1996) used a Moore-Penrose pseudo-inverse of the 3D sensitivity matrix. Several subsequent authors have extended this approach to a regularized Gauss-Newton inverse (e.g. Blue *et al* 2000, Borsic *et al* 2010). Another mathematically interesting approach uses the D-bar scattering transform (Knudsen *et al* 2009). Most algorithms use some type of regularization technique to allow control of the resulting compromise between robustness to noise and resolution in the reconstructed images.

Since its publication (Adler *et al* 2009), GREIT (Graz consensus Reconstruction algorithm for EIT) has become popular in lung EIT applications. The original formulation and implementation was limited to cylindrical geometries with planar electrode arrangements, but subsequent adaptations facilitate reconstructions on arbitrary geometries (Grychtol *et al* 2012). Recently, Ahn *et al* (2014) proposed and tested in a 360-electrode micro-EIT setup an extention of the GREIT algorithm to 3D.

This overview shows that 3D EIT reconstruction algorithms are both required and available. Why, then, are they so rarely used in human and animal experimental and clinical studies? We suggest two main explanations. First, the detailed performance of 3D EIT is not understood, including what specific advantages it offers versus the number of extra electrodes required. For example, questions such as the vertical sensitivity or resolution of a given configuration, how far apart the electrode planes should be, what stimulation and measurement patterns are best, and what kinds of imaging artefacts can be expected? This lack of information is partially caused by our second explanation: a lack of available hardware and software. Few EIT systems have been made specifically for 3D imaging, and it is difficult to reconfigure other systems for this purpose. Additionally, the application of such a large number of electrodes is inconvenient without multiple electrode bands. From an imaging point of view, there has been a lack of easy-to-use tools to adapt 3D EIT reconstruction to generic body shapes and electrode configurations.

In this paper, our goal is to provide tools that address these requirements. We

reformulate the GREIT algorithm to make the parameters associated with the vertical resolution explicit. Using this formulation, we explore the vertical sensitivity of 3D EIT measurements and reconstructions. All software and FEM models are available under an open-source license as part of EIDORS version 3.8 (Adler *et al* 2015a).

2. Methods

In the following sections, we develop the formulation of regularized linear difference EIT reconstruction, and show the GREIT algorithm and its relationship to other regularized approaches such as the Gauss-Newton formulation. We then develop an extension of GREIT to 3D imaging, and describe the figures of merit appropriate for 3D EIT. Finally, a model to study the forward and reconstruction sensitivity is introduced, and an open-source software implementation is developed and discussed.

2.1. GREIT formulation

The formulation developed here yields an identical expression to that of Adler *et al* (2009); however, this formulation is simpler, and makes relationship of GREIT to other Bayesian approaches clear. The notation is similar, but not identical, to the previous work. We consider a body with a baseline (i.e. before changes, signified as (*b*)) conductivity distribution parameterized as $\boldsymbol{\sigma}^{(b)}$, where parameters are normally the piecewise constant conductivities within each element of a finite element model (FEM).

Linear difference EIT is sensitive to a change, $\Delta\boldsymbol{\sigma} = \boldsymbol{\sigma}^{(a)} - \boldsymbol{\sigma}^{(b)}$, between *after*, $\boldsymbol{\sigma}^{(a)}$, and *before*, $\boldsymbol{\sigma}^{(b)}$. Changes can occur over time (time-difference EIT, tdEIT) or frequency (frequency-difference EIT, fdEIT). A frame of voltage measurement data, **v**, is acquired through a set of stimulation and measurement patterns. The generation of voltage data is modelled by the forward problem, $F(\cdot)$, typically using a FEM, which yields two data frames: $\mathbf{v}^{(b)} = F(\boldsymbol{\sigma}^{(b)})$ and $\mathbf{v}^{(a)} = F(\boldsymbol{\sigma}^{(b)} + \Delta\boldsymbol{\sigma})$. Based on two frames of measured data, a measurement change vector, **y**, can be defined for difference EIT $(y_i = v_i^{(a)} - v_i^{(b)})$ or normalized-difference EIT $(y_i = v_i^{(a)}/v_i^{(b)} - 1)$. Here, subscripts indicate selection of the an element from a matrix, so the ith element of $\mathbf{v}^{(b)}$ is $v_i^{(b)}$.

Image reconstruction in difference EIT seeks to reconstruct an image, $\hat{\mathbf{x}}$, parameterized over elements or voxels, from the difference data, **y**. In 3D EIT, the imaged region, $\hat{\mathbf{x}}$, is normally smaller than the forward-modelled region, because, far from the electrodes, there are areas of such low sensitivity that they cannot be reconstructed reliably, but which have enough effect that they should be modelled in the forward problem. This situation differs from 2D EIT, where it is common for $\hat{\mathbf{x}}$ to represent the same shape as $\boldsymbol{\sigma}$. In so called 2.5D approaches, $\hat{\mathbf{x}}$ is limited to a slice, but $\boldsymbol{\sigma}$ represents a change through the entire vertical dimension crossing the slice.

In addition, the forward model requires a high accuracy (and a corresponding high density of mesh parameterization) in areas of high electric field (such as near the electrodes). The inverse parameterization does not benefit from an increased mesh

density near the electrodes, since the spatial variation of the underlying conductivity change is not different in these regions. To allow different forward and inverse parameterizations, the relationship between forward and inverse parameterization is modelled by a coarse-to-fine map, $\mathbf{M}$, which projects $\Delta\boldsymbol{\sigma} = \mathbf{M}\mathbf{x}$. Each element, $\mathbf{M}_{i,j}$, thus represents the volume fraction of each forward-model region i contained within the inverse model region j.

We are interested in linear reconstruction algorithms for difference EIT, in which image reconstruction can be represented by a reconstruction matrix, $\mathbf{R}$, by which the reconstructed image is calculated from the difference data as

$$\hat{\mathbf{x}} = \mathbf{R}\mathbf{y}. \tag{1}$$

The GREIT approach defines the best reconstruction matrix over a set or distribution of "training" targets, $\mathbf{t}^{(i)}$. $\mathbf{R}$ thus minimizes an error ϵ^2,

$$\epsilon^2(\mathbf{R}) = \mathop{\mathrm{E}}_{w}\left[\|\mathbf{x} - \mathbf{R}\mathbf{y}\|^2\right] \tag{2}$$

where the expectation, $\mathrm{E}_w[\cdot]$ is over the training target distribution. For each "training" target, the corresponding data, $\mathbf{y}$, and a "desired" image, $\mathbf{x}$, are generated. The choice of a 2-norm allows for a linear calculation for $\mathbf{R}$. w is the weight assigned to each target, $\mathbf{t}$, to represent the importance of its contribution.

When "training" is defined by a distribution, $\mathrm{E}_w[\cdot]$ is weighted by w. When training is defined by a set of N targets, the expectation is modelled as an average, $\mathrm{E}_w[x] = \frac{1}{N}\Sigma_{i=1}^{N}w_i x_i$. Values of w are normalized so their average is 1.

The reconstruction matrix is chosen by minimizing ϵ^2, and setting $\partial\epsilon^2(\mathbf{R})/\partial\mathbf{R} = 0$. Using the commutative property of the expectation operator and the identity $\frac{\partial}{\partial\mathbf{R}}\|\mathbf{x} - \mathbf{R}\mathbf{y}\|^2 = -2(\mathbf{x} - \mathbf{R}\mathbf{y})\mathbf{y}^T$ from Petersen and Pedersen (2012), we get

$$\frac{\partial}{\partial\mathbf{R}}\epsilon^2 = \mathop{\mathrm{E}}_{w}\left[\frac{\partial}{\partial\mathbf{R}}\|\mathbf{x} - \mathbf{R}\mathbf{y}\|^2\right] = -2\mathop{\mathrm{E}}_{w}\left[(\mathbf{x} - \mathbf{R}\mathbf{y})\mathbf{y}^T\right] = 0 \tag{3}$$

We thus have

$$\mathop{\mathrm{E}}_{w}\left[\mathbf{x}\mathbf{y}^T\right] - \mathbf{R}\mathop{\mathrm{E}}_{w}\left[\mathbf{y}\mathbf{y}^T\right] = 0 \tag{4}$$

from which the GREIT reconstruction matrix, $\mathbf{R}$, can be calculated

$$\mathbf{R} = \mathop{\mathrm{E}}_{w}\left[\mathbf{x}\mathbf{y}^T\right]\left(\mathop{\mathrm{E}}_{w}\left[\mathbf{y}\mathbf{y}^T\right]\right)^{-1} \tag{5}$$

Equation (5) can be calculated in two ways, depending on whether training data are defined as a set or as a distribution.

2.1.1. GREIT defined from training sets. A set of N_t training samples are defined at a set of locations to cover the region to be reconstructed. For each sample, $\mathbf{t}_i$, a desired image, $\mathbf{x}_i$ is defined. Here, we use the subscript i to signify the ith vector in the set. This desired image covers a larger region than the point locations of the training samples; this is motivated by the inherently limited resolution of EIT. For a 16-electrode system, a recommendation of 20% of the medium diameter was given by Adler *et al* (2009).

For each sample, $\mathbf{t}_i$, the corresponding difference data, $\mathbf{y}_i$ are generated. Typically, these are calculated using a numerical model (such as a FEM); however, it is also possible to directly measure, $\mathbf{y}$. Gaggero *et al* (2014) used a robot to place targets in a tank phantom, and showed the resulting images were improved over simulated values. This improvement was explained as reflecting the fact that measurements also include the specific system inaccuracies which are not part of the numerical model.

To model system noise, a set of N_n additive noise samples are simulated or acquired.

$$\underset{w}{\mathrm{E}}\left[\mathbf{y}\mathbf{y}^T\right] = \frac{1}{N_t}\sum_{i=1}^{N_t} w_i \, \mathbf{y}_i\mathbf{y}_i^T + \frac{1}{N_n}\sum_{i=1}^{N_n} \mathbf{n}_i\mathbf{n}_i^T \tag{6}$$

$$\underset{w}{\mathrm{E}}\left[\mathbf{x}\mathbf{y}^T\right] = \frac{1}{N_t}\sum_{i=1}^{N_t} w_i \, \mathbf{x}_i\mathbf{y}_i^T \tag{7}$$

The sum, $\Sigma_{i=1}^{N_n}\mathbf{n}_i\mathbf{n}_i^T = \boldsymbol{\Sigma}_n$, estimates the noise covariance, $\boldsymbol{\Sigma}_n$. It is based on an average weight, $w = 1$, because noise samples are independent of target location. If an *a priori* estimate of the noise covariance is available, this value is used directly. It is most common to assume noise samples are independent and uncorrelated across measurements, and thus the covariance is a scaled identity matrix, $\boldsymbol{\Sigma}_n = \sigma_n^2\mathbf{I}$. However, in practice, noise may reflect many other correlated contributions, such as crosstalk between channels. Electrode movement can also be represented as a correlated noise (Adler and Lionheart, 2011).

The sums, $\Sigma_{i=1}^{N_t}w_i\mathbf{y}_i\mathbf{y}_i^T$, and $\Sigma_{i=1}^{N_t}w_i\mathbf{x}_i\mathbf{y}_i^T$, are weighted by w_i to represent the importance of each training sample i to the reconstructed image. If errors at a particular position in an image are more serious for some reason, w_i for $\mathbf{t}_i$ at those positions is increased. The reconstruction matrix will then "prefer" greater accuracy in these locations. The effect of weighting can also be achieved by the selection of training targets. By choosing more samples within a given image region, the effective w for targets in that area is increased.

2.1.2. GREIT defined from distributions. Given a training distribution $\mathbf{t} \sim \mathcal{N}(0, \boldsymbol{\Sigma}_t)$ we have the distribution of training targets, $\mathbf{x}$, and measurements, $\mathbf{y}$,

$$\mathbf{x} = \mathbf{D}\mathbf{t} \tag{8}$$

$$\mathbf{y} = \mathbf{J}\mathbf{t} + \mathbf{n} \tag{9}$$

where $\mathbf{D}$ is the "desired image" matrix, which maps each training sample location onto the larger desired image region as discussed above. $\mathbf{J}$ is the Jacobian or sensitivity matrix of the forward model, $F(\cdot)$. Including a coarse-to-fine mapping, $\mathbf{J} = \mathbf{J}_f\mathbf{M}$, where $\mathbf{J}_f$ is the Jacobian defined on the finer mesh discretization. Noise, $\mathbf{n}$, is distributed as $\mathbf{n} \sim \mathcal{N}(0, \boldsymbol{\Sigma}_n)$.

$$\underset{w}{\mathrm{E}}\left[\mathbf{y}\mathbf{y}^T\right] = \mathbf{J}\underset{w}{\mathrm{E}}\left[\mathbf{t}\mathbf{t}^T\right]\mathbf{J}^T + \underset{w}{\mathrm{E}}\left[\mathbf{n}\mathbf{n}^T\right] = \mathbf{J}\boldsymbol{\Sigma}_t^*\mathbf{J}^T + \boldsymbol{\Sigma}_n \tag{10}$$

$$\underset{w}{\mathrm{E}}\left[\mathbf{x}\mathbf{y}^T\right] = \mathbf{D}\underset{w}{\mathrm{E}}\left[\mathbf{t}\mathbf{t}^T\right]\mathbf{J}^T \qquad = \mathbf{D}\boldsymbol{\Sigma}_t^*\mathbf{J}^T \tag{11}$$

where $\boldsymbol{\Sigma}_t^*$ is the effective covariance of the training targets when weighted by w. The noise covariance $\boldsymbol{\Sigma}_n$ is not affected by weighting, since we assume noise is independent of target location.

Thus the reconstruction matrix from (5) is

$$\mathbf{R} = \mathbf{D}\boldsymbol{\Sigma}_t^*\mathbf{J}^T\left(\mathbf{J}\boldsymbol{\Sigma}_t^*\mathbf{J}^T + \lambda\boldsymbol{\Sigma}_n\right)^{-1} \tag{12}$$

where, in order to achieve a desired noise performance, the noise covariance is scaled by a hyperparameter, λ. The value of this hyperparameter is found by bisection search until the noise performance of the reconstruction matrix matches a specified noise figure, which was recommended to be 0.5.

Equation (12) can be shown to be equivalent to a Gauss-Newton reconstruction matrix, $\mathbf{R}_{GN}$, obtained by Generalized Tikhonov regularization to minimize the norm

$$\|\mathbf{t} - \mathbf{J}\mathbf{y}\|_{\mathbf{W}}^2 + \|\mathbf{t}\|_{\mathbf{Q}}^2 \tag{13}$$

to calculate a reconstructed $\hat{\mathbf{t}} = \mathbf{R}_{GN}\mathbf{y}$, and thus a reconstructed desired image $\hat{\mathbf{x}} = \mathbf{D}\hat{\mathbf{t}} = \mathbf{D}\mathbf{R}_{GN}\mathbf{y}$.

From (13),

$$\mathbf{R}_{GN} = \left(\mathbf{J}^T\mathbf{W}\mathbf{J}^T + \mathbf{Q}\right)^{-1}\mathbf{J}^T\mathbf{W} = \mathbf{Q}^{-1}\mathbf{J}^T\left(\mathbf{J}\mathbf{Q}^{-1}\mathbf{J}^T + \mathbf{W}^{-1}\right)^{-1} \tag{14}$$

which is equivalent to the GREIT formation if Tikhonov parameters are chosen such that $\mathbf{W} = \boldsymbol{\Sigma}_n^{-1}$, and $\mathbf{Q} = (\boldsymbol{\Sigma}_t^*)^{-1}$.

2.1.3. Definition of desired images One key parameter influencing the properties of the GREIT reconstruction matrix is the definition of the desired images. In Adler *et al* (2009), desired images were defined as circles centered at the point targets' position, with an inner circular zone where the amplitude is flat and a zone outside a larger circular boundary where the amplitude is zero. Between the two circles, the amplitude is required to "gradually decrease".

We propose a formalization of the desired image definition by means of a sigmoid function of position

$$f(\mathbf{r}) = \left(1 + \frac{e^{s|\mathbf{r}-\mathbf{r}_0|}}{e^{sR}}\right)^{-1}, \tag{15}$$

where $\mathbf{r}$ is the position vector in 2- or 3D, $\mathbf{r}_0$ is the target center, R is the desired radius and s is a scalar controlling the blur, as illustrated in Grychtol *et al* (2015). The desired image $\mathbf{x}$ is the discretization of $f(\mathbf{r})$ onto the image. Each image pixel or voxel is assigned the value of $f(\mathbf{r})$ integrated over the volume (area in 2D), which we implement numerically by evaluating the function at a distribution of interior points.

2.2. Figures of Merit

As described in the previous section, the reconstruction matrix is determined by the choice of training targets, desired images, and noise characteristics. Since this selection involves the choice of several tunable parameters, Adler *et al* (2009) proposed a set of

figures of merit by which the perfomance of the reconstruction matrix may be evaluated. In this section, these figures are reviewed, and modifications proposed for evaluation of 3D algorithms.

For evaluation, "point" evaluation targets are introduced, $\mathbf{t}_e$, for which the corresponding difference data, $\mathbf{y}_e$, are either simulated or measured, and a reconstructed image, $\hat{\mathbf{x}}_e = \mathbf{R}\mathbf{y}_e$, calculated. For notation, $\mathbf{t}_e$ is at position vector $\mathbf{r}_t$, and has a corresponding desired image, $\mathbf{d}_e$. From $\hat{\mathbf{x}}_e$ a $\frac{1}{4}$-maximum image, $\hat{\mathbf{x}}_q$, is calculated. Each element i of $\hat{\mathbf{x}}_q$ has value 1 if the corresponding $(\hat{\mathbf{x}}_e)_i \geq \frac{1}{4}\max(\hat{\mathbf{x}}_e)$, and zero otherwise. Figures of merit for amplitude, position, shape, and noise are defined. A vector, $\mathbf{a}$, representing volume (or area) of each reconstructed image element is defined; for a voxel- or pixel-based reconstruction, elements of $\mathbf{a}$ are equal.

2.2.1. Figures of merit for reconstructed amplitude. The amplitude response (AR) is the normalized global image sum, $\mathrm{AR} = \frac{1}{k}\mathbf{a}^T\hat{\mathbf{x}}_e$, where the normalization k is defined so that AR is proportional to target volume and conductivity for small targets. A uniform AR across the imaged plane was identified as the most important parameter. However, in 3D this is not possible or desirable far from the electrode planes. Instead, we seek a uniform AR within electrode layer region.

Since AR is a global image parameter, we also define an amplitude response in the target region, $\mathrm{AR_T}$, which represents AR only in the desired image region. Thus, $\mathrm{AR_T} = \frac{1}{k}\mathbf{a}^T\mathrm{diag}(\mathbf{d}_e)\hat{\mathbf{x}}_e$, and represents the amplitude of the part of the reconstructed image which is correctly located within the desired image, and thus exclude image artefact regions.

2.2.2. Figures of merit for reconstructed position. Errors in the reconstructed position are measured by the position error, $\mathrm{PE} = r_t - r_q$, where $r_t = |\mathbf{r}_t|$ is the distance of the target from the image centre, and $r_q = |\mathbf{r}_q|$ is the distance of the reconstructed area from the image centre. PE is positive for a reconstructed image which is too close to the boundary, and negative when it is too close to the body centre. In 3D, a scalar PE is less informative, so Cartesian components, $(\mathrm{PE}_x, \mathrm{PE}_y, \mathrm{PE}_z)$, are defined from the vector $\mathbf{r}_t - \mathbf{r}_q$. In Adler *et al* (2009), $\mathbf{r}_q$ is the center of gravity of $\hat{\mathbf{x}}_q$. Instead, we propose to use the centre of gravity of the amplitude-scaled $\frac{1}{4}$-maximum area, $\mathrm{diag}(\hat{\mathbf{x}}_e)\hat{\mathbf{x}}_q$. This amplitude-scaled region is more visually representative of the location of the reconstructed image.

2.2.3. Figures of merit for reconstructed shape. Three figures of merit are defined to describe the shape of the reconstructed region. The most important is the resolution, defined on a 2D slice as $\mathrm{RES} = \sqrt{A_q/A_0}$, where A_q is the area of the $\frac{1}{4}$-maximum image, $\hat{\mathbf{x}}_q$, and A_0 is the whole slice area. In 3D, there is a need to define resolutions in each dimension (RES_x, RES_y, and RES_z). We propose a full-width quarter-maximum (FWQM) definition in each dimension. Thus, for example, RES_z is the distance between

the lower and upper $\frac{1}{4}$-maximum point in the graph of the global image sum along the z-axis.

For 3D GREIT, ringing (RNG) and shape deformation (SD) are defined similarly to their 2D definitions. First, a volume V_q is defined as the volume of the 3D $\frac{1}{4}$-maximum image, $\hat{\mathbf{x}}_q$. A sphere, S_q, is defined of volume V_q centred at the target location, $\mathbf{r}_t$. SD is calculated as the fraction of the volume of V which is not within S. SD becomes large as the shape of the reconstructed region differs from a sphere. This difference in shape will also be reflected by differences between the resolution in the cartesian axes.

The ringing measures whether reconstructed images show areas of opposite sign surrounding the main reconstructed target area. RNG is defined as the ratio of image amplitude of the opposite sign outside S to the image amplitude amplitude within S. The best performance is that RNG be low and uniform, since regions with an opposite sign can be misinterpreted in an image.

2.2.4. Figures of merit for reconstructed noise. The noise performance of GREIT is defined by the amplitude of the noise distribution, $\boldsymbol{\Sigma}_n$. This is measured by the noise figure, $\mathrm{NF} = \mathrm{SNR}[\hat{\mathbf{x}}]/\mathrm{SNR}[\mathbf{y}]$, which is the ratio of SNR in the reconstructed image to that in the difference data. Here the signal to noise ratio, $\mathrm{SNR}[\cdot] = \mathrm{mean}[\cdot]/\mathrm{std}[\cdot]$, is defined as the ratio of image and signal amplitude to standard deviation, rather than the more usual energy to variance ratio.

3. Evaluation

The developed reconstruction algorithm was evaluated in two ways: using a tank phantom, and using a detailed FE model of the thorax from which the sensitivity of various patterns could be evaluated.

3.1. Tank phantom

A cylindrical tank phantom was used and filled with a saline solution. This phantom is composed of an acrylic glass cylinder with an internal diameter of 290 mm and a height of 375 mm. The phantom has four rows of 32 4 mm gold-plated electrodes each, of which upper and lower rows were used. The electrodes were thus spaced by 70 mm. The phantom was filled with 22 L water mixed with 200 g of NaCl. A non-conductive spherical test object of 45 mm diameter and 50 ml volume was used.

Using a test harness, the ball was moved from the centre to the boundary of the tank in three different layers, corresponding to the centre (middle between the planes), half way from the centre to the upper plane, and in line with the upper plane.

Data were acquired using the Pioneer Set (Swisstom AG, Landquart, Switzerland). Thirty two electrodes were placed with odd numbered electrodes on the upper ring and even numbered electrodes on the bottom ring, such that electrode #2 is directly below #1. The acquisition protocol was using a "skip 4" pattern on both stimulation

and measurement. Data were acquired first for a homogeous phantom, and then for at least 100 frames at each object position. Data frames were averaged at each scenario to reduce system noise.
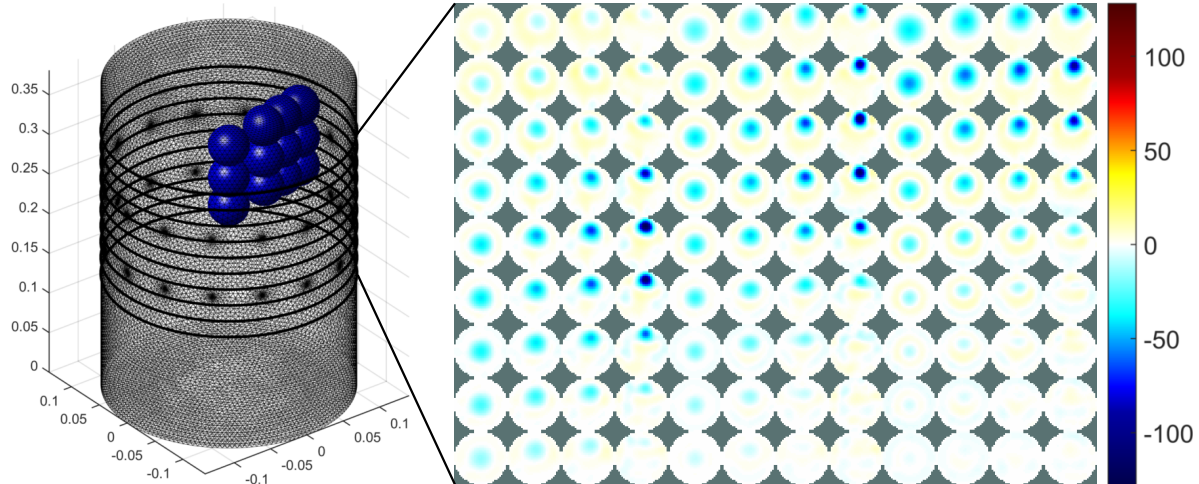

Figure 1: *Left:* FE model of a water tank showing cut planes between voxel layers and positions of a non-conductive spherical target (axes in meters). *Right:* images reconstructed using the proposed algorithm. Each row corresponds to one voxel layer, and each column to a different target position.

Reconstructions of tank data are shown in figure 1. On the left, the finite element model of the tank is shown along with the positions of the non-conductive ball target. At right, the reconstructed images are shown in each column. Each 3D reconstructed image is divided into 9 horizontal cut planes. The images show the ability of 3D GREIT to successfully differentiate the vertical position of the target.

Variations in vertical and radial position of a non-conductive spherical target are successfully reconstructed. As expected, amplitude response and resolution fall toward the long axis of the tank and away from the electrode plane. On the other hand, ringing seems to be stronger in the electrode planes.

3.2. Thorax finite element model

A detailed FEM of the thorax was created, with the goal of providing a test framework for this study, as well as a representative thorax FEM on which future simulation work can be done. The basic shape was defined as part of Adler *et al* (2009), using the the male visible human body dataset (Ackerman 1998). The provided photographic images (of vertical spacing 20 mm) were used to generate the surface models from which the finite element meshes were generated, similarly to the method described in Tizzard *et al* 2005. Using this volume mesh, the surface mesh was extracted, electrodes placed on the surface and the volume remeshed as desribed by Grychtol and Adler (2013). Regions for the heart and lungs were defined based on ellipsoid geometries in anatomically appropriate regions. The diaphragm was also modelled as an ellipsoid

region surrounding the abdomen. The model is shown in figure 2, and is available in the EIDORS `mk_library_model` function.

Multiple electrodes are defined onto the surface of the FEM in order to allow for evaluation of different electrode placement and stimulation strategies; the model contains 86843 nodes and 425913 elements. At each electrode a highly refined mesh is defined in order to better model the local current distribution and sensitivity. A central electrode plane is defined corresponding to the $6^{th} - 7^{th}$ intercostal space at the parasternal line with 32 electrodes. Above and below this central plane by 25 mm, planes of 16 electrodes are defined. Using this model, it is possible to select the electrodes used within EIDORS, by using only those which correspond to a simulated position.
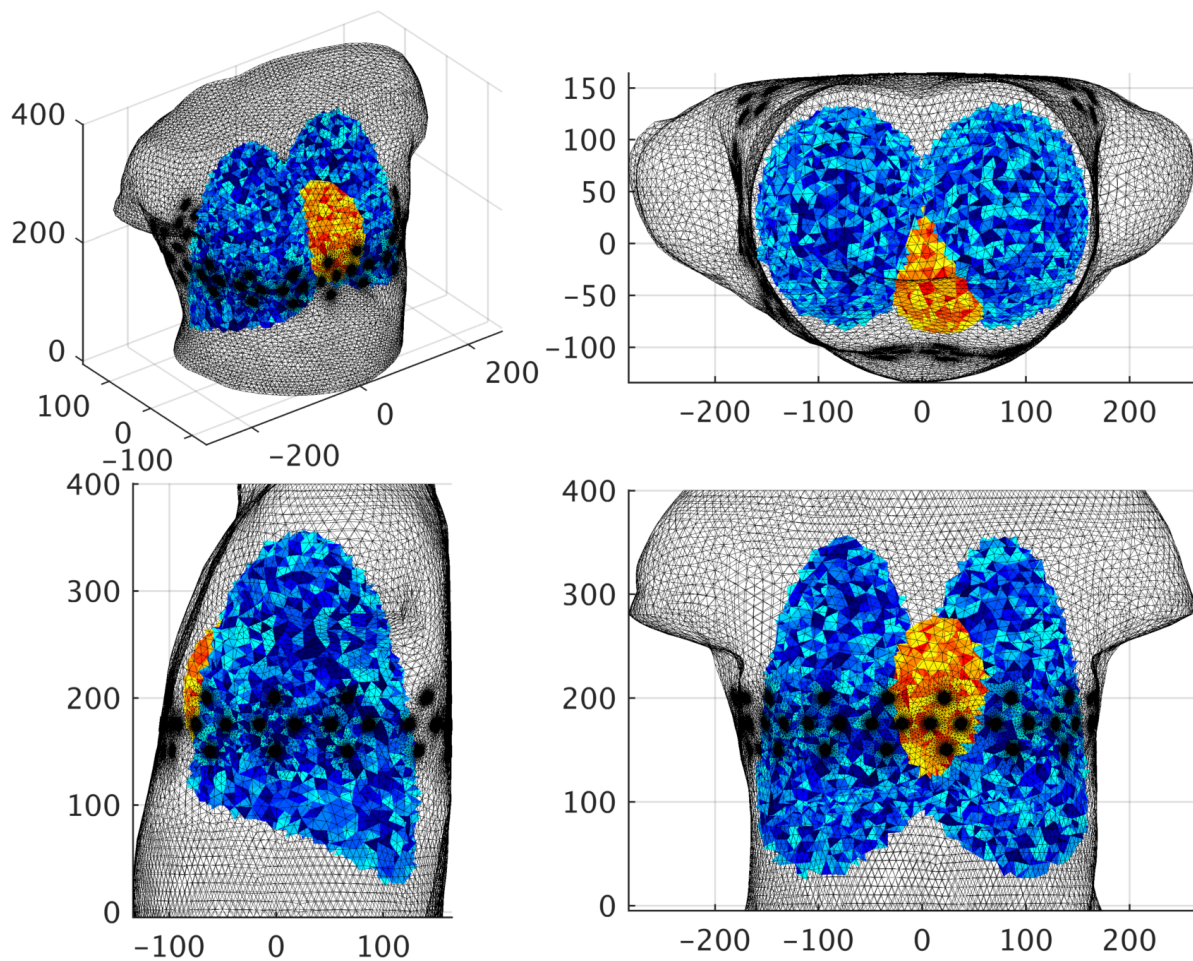

Figure 2: Detailed male thorax FEM based on the visible human dataset. Four views are shown (axes in millimeters). Lung (blue) and heart (red) are illustrated with respect to transparent (other tissues). Three layers of electrodes are visible on body surface as regions with refined mesh.

One important question in 3D EIT is the selection of stimulation and measurement patterns. There is a much richer choice of such patterns than in a single plane placement, and many questions are open, such as whether there is a trade-off between vertical and

horizontal resolution and sensitivity in the 3D image. While we are not able to address this issue in detail, we illustrate a way forward using the 3D FEM and imaging tools we describe. Using the thorax FEM described, we calculated the sensitivity for forward and inverse solutions. Stimulations were calculated for a homogeneous model, and for a case with physiologically realistic organ conductivities. Compared to soft tissue conductivity, σ, lung region conductivity was set to be $0.20 \times \sigma$, while the heart was set to $1.5 \times \sigma$. stimulation and measurement patterns. For each model, a selection of stimulation pattern strategies was used, as shown in figure 3. The three patterns chosen were motivated by Graham and Adler (2007) and designed to explore the space of patterns sensitive to horizontal and vertical gradients. The planar pattern is primarily sensitive to horizontal gradients, since most stimulus current travels horizontally. The odd/even pattern is more sensitive to vertical gradients; all stimulation and measurement patterns cross the centre plane. Finally, the square pattern has half of its stimulations in a single plane and half which cross the centre. All patterns simulated here can be implemented with an adjacent drive EIT system by switching the electrode positions and then reordering the data.
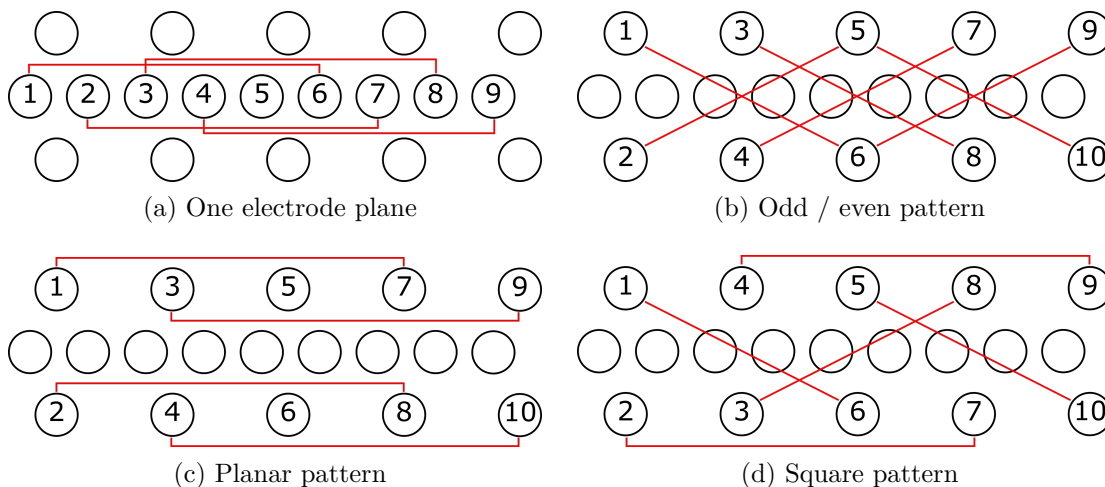

Figure 3: Electrode stimulation and measurement configurations considered, assuming that a pair-drive EIT system has an equal "skip" value for both stimulation and measurement pairs: (a) One electrode plane with skip 4, (b) Two planes with an even (4) skip (Odd/even), (c) Two planes with an odd (5) skip (Planar), (d) Square pattern (skip 4).

3.3. Forward and Inverse Sensitivity

For interpretation of EIT images, it is important to understand the spatial region to which EIT is sensitive. In 3D EIT, it is expected that the sensitive region will depend on the electrode placement, stimulation pattern, and other anatomical factors related to the shape of the thorax and the presence of inhomogeneities, especially the lungs.

We distinguish the concepts of forward- and inverse-sensitivity regions. Two areas with equal forward sensitivity cause an equal change in amplitude of the difference signal, $\|\mathbf{y}\|$. However, the reconstruction process will not necessarily project these to equal amplitude reconstructions, $\mathbf{x}$. Instead, two regions of equal inverse sensitivity will have equal amplitude resonse.

Forward sensitivity, S_i, was calculated, for each FEM element, i, as the root mean square of the sensitivity Jacobian, and then normalized to the volume of that element, V_i. Thus, $S_i = \frac{1}{V_i}\|\mathbf{J}_i\|$, where $\mathbf{J}_i$ is the ith column of the Jacobian, $\mathbf{J}$. The distribution of sensitivity is shown in figure 4 for one- and two electrode planes using an adjacent (skip 0) and larger skip patterns. The most uniform sensitivity is achieved with two planes and a larger skip.
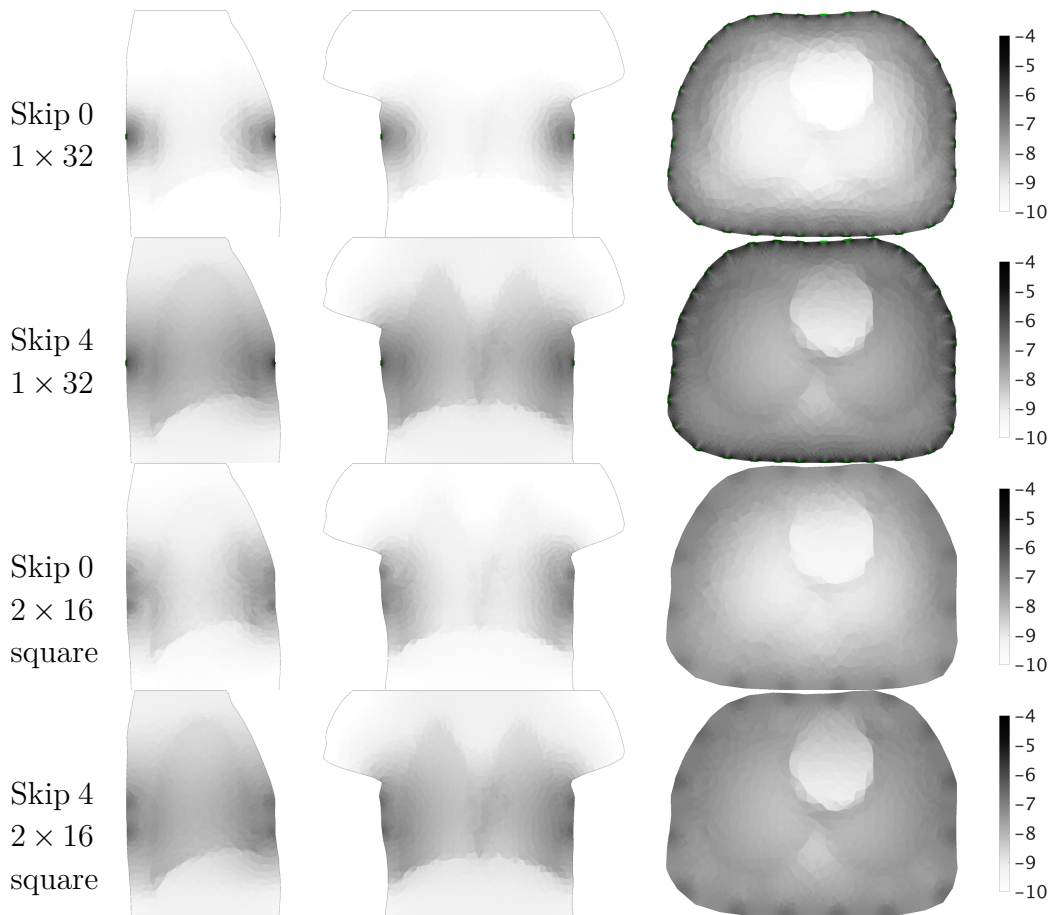

Figure 4: Forward sensitivity of thorax model with lung and heart regions. Darker image regions indicates increasing log sensitivity. For each row, the indicated skip pattern and electrode arrangement (layers×electrodes/layer) is used. Image columns from left to right: saggital ($x = -75$ mm), coronal ($y = 50$ mm), and transverse (at the centre electrode plane). All images use the same colour scale.

GREIT inverse models were defined for each stimulation pattern, including the 2D (single plane of 32 electrodes) and 3D (two planes of 16 electrodes) cases. In 2D, the

data are reconstructed onto 690 square pixels of a 32×32 pixel grid defined at the plane of electrodes. In 3D, the volume of the model is span by a $52 \times 33 \times 39$ grid of cubic voxels, of which 29886 intersect with the model and are used for reconstruction. The grid of voxels is chosen such that at the middle electrode plane the pixels and voxels align exactly. The side length of each voxel and pixel was 10.959 mm. For all inverse models, the targets used for calculating the GREIT reconstruction matrix were spherical (circular for 2D) contrasts with a diameter of 40 mm placed at the center of each voxel (pixel in 2D). The weight hyperparameter, equal for all targets, was chosen such as to achieve a noise figure of 1.0 at the center of the lung objects at the middle electrode plane.

To illustrate the inverse sensitivity, we extend to three dimensions the concept of amplitude response maps described in Grychtol *et al* (2012). Briefly, the difference measurements caused by a number of small spherical targets (radius 10 mm) with a conductivity contrast of $0.01 \times \sigma$ were calculated and reconstructed with each inverse model. The targets were arranged in several cut planes in a regular grid with 10 mm spacing. From these target positions, an amplitude response map was created by assigning each target position the amplitude response value of the reconstructed image of that individual target.

3.4. Reconstruction sensitivities

The primary motivation for using a 3D placement of EIT electrodes is to control the imaging volume to which EIT is sensitive. Using the 3D GREIT formulation and the thorax model developed, we present an inital exploration of this question. We identify three main factors influencing the sensitivity for two electrode layers:

- *Layer separation:* The reconstruction volume and measurements become more independent as layers are further separate. We consider a layer separation of 50 mm and compare it to a single electrode layer (of 32 electrodes).

- *Stimulation and measurement pattern:* As the active electrodes are further apart, the sensitive region is driven further into the body (Adler *et al* 2011). This effect is expected to occur also in 3D, but with an additional constraint: the vertical resolution is likely to depend on what fraction of patterns cross the central area.

- *Body inhomogeneities:* The presence of conductivity inhomogeneities in the thorax disturbs the pattern of current flow, shielding the inner lungs and heart (Grychtol and Adler 2014).

Simulations were performed over a range of values of the indicated factors, and the figures of merit calculated. In figure 5, the amplitude response map is shown for a lung-filled model for a single- or two-layer stimulation and for two stimulation and measurement patterns and with different skip distances. A large difference is visible between the patterns, using an adjacent (skip 0) pattern, the sensitive region remains close to the electrodes. For the increased skip (electrodes approximately 45° apart), the
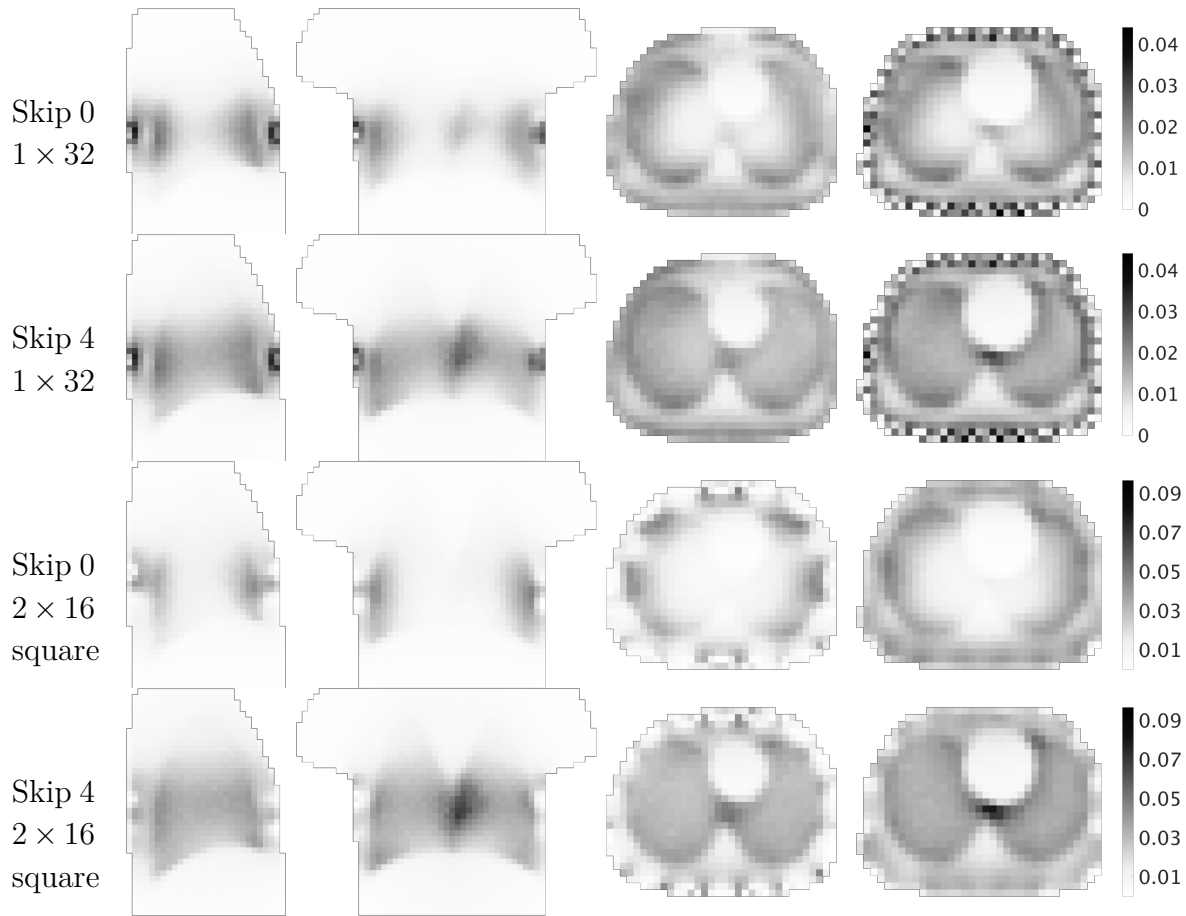
Figure 5: Amplitude response map of GREIT reconstruction in a thorax model with lung and heart regions. Darker regions indicate increasing absolute amplitude response. For each row, the indicated skip pattern and electrode arrangement (layers×electrodes/layer) is used. Image columns from left to right: saggital ($x = -75$ mm), coronal ($y = 50$ mm), and transverse at the lower and centre electrode planes. Images for the 1×32 and 2×16 arrangements use different, but consistent, colour scaling.

sensitive region is much more uniform. With two layers, the uniformity of the sensitivity is improved across the thorax.

The uniformity of the amplitude response map is significantly improved using two electrode layers and a larger skip pattern. While the square pattern is shown, the image from the odd/even and planar arrangements were similar. It is also interesting to compare the amplitude response map for a homogeous thorax (figure 6), which is again much more uniform in the central transverse plane.
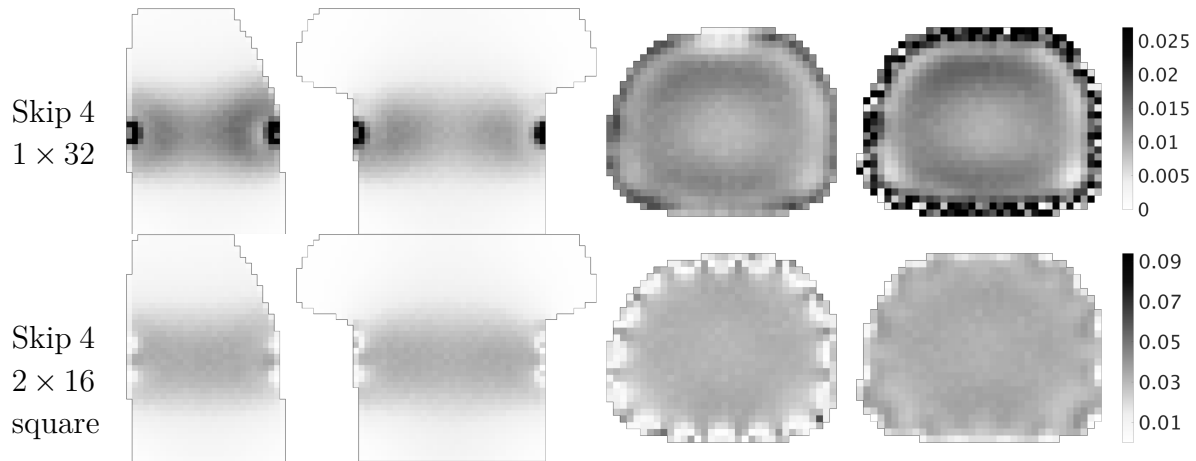
Figure 6: Amplitude response map for homogenous thorax model, in comparison to figure 5. Images are scaled such that the value in the centre of the model is the same.

4. Discussion

This paper extends the GREIT framework of Adler *et al* (2009) to 3D imaging using several electrode planes. For lung imaging, there are two main motivations for such image reconstruction. First, many common lung pathologies are inherently inhomogeneous and should thus be imaged volumetrically so there is a better chance of seeing the relevant areas. Also, even if a volume image is not desired, the "slice" given by a single plane system represents a poorly constrained lens-shaped region. In this case, 3D image reconstruction is of interest as a way to reject out of plane contributions and deliver a better 2D slice.

By itself, 3D EIT imaging is not novel; early work by Rabbani and Kabir (1991) considered the volumetric sensitivity of EIT; 3D reconstruction was first shown by Metherall *et al* (1996) for difference EIT, but has since also been used in many absolute EIT algorithms. GREIT has also recently been extended to 3D by Ahn *et al* (2014). Given all this work on 3D EIT, it is surprising that almost all thoracic EIT imaging is still done with a single plane of electrodes. This paper is motivated to make the contributions to address what we perceive as holding EIT back: 1) easy to use 3D algorithm tools, and 2) an evaluation framework to understand when, and how much, benefit is available from 3D imaging.

To address the first requirement, the GREIT algorithm is reformulated to make clear its relationship to other regularized linear difference approaches, and specifically the Gauss-Newton algorithm. While the formulation is equivalent, GREIT makes its dependence on the parameters of the "training" set explicit. With parameters formulated as training and desired image sets, it is hopefully more clear how to adjust the algorithm to meet various figures of merit. This algorithm has been made available as part of EIDORS 3.8 and its software interface is detailed (**??**).

To address the second requirement, we develop a framework for evaluation of

the sensitivity and reconstruction figures of merit for various two-layer electrode configurations. A thorax FEM with electrode refinement is developed, and a number of electrode positions and stimulation and measurement configurations are evaluated. While this analysis was not comprehensive, one clear observation is that two-layer EIT electrode configurations have significantly more uniform sensitivity profiles through the body. It is worth noting that for 3D imaging, an accurate knowledge of relative positions of the electrode planes is especially important (Bayford *et al* 2008). Errors in model of electrode plane separation would corrupt the image reconstruction accuracy.

While our results show promise, it is also clear that there are many aspects of 3D EIT with two electrode layers that are poorly understood and need clarification: How far apart should the layers of electrodes be? What skip distance should be used for pair-drive stimulation and measurement patterns? Should all the pair-drive patterns cross the centre plane, or is *z*-resolution sufficiently improved when only a fraction of them do so? Specifically for the GREIT algorithm, we ask: What is the desired image for an out-of-plane target? How, if at all, should the desired image amplitude be affected by the measurement sensitivity? How many targets are necessary, and how should they be distributed? If non-uniform voxel sizes are used (especially off-plane in the *z*-direction) this will impose a spatial low-pass regularization effect; is this effect desired and when? If not, then there is a high computational cost of calculation of the 3D GREIT reconstruction matrix.

In summary, this paper develops the formulation of the GREIT algorithm for 3D EIT with multiple electrode planes and shows promising results in terms of more uniform sensitivity across the chest. Given these results, we argue that patient-friendly multiple-plane EIT systems should be developed to make these technical advantages available in the clinic.

Appendix A. Implementation

Software to implement 3D GREIT has been developed and an easy-to-use interface released as part of EIDORS version 3.8 (Adler *et al* 2015a). An example of a functioning set of code is given in listing 1.

First, a forward model (`fmdl`) must be defined (line 1), which, in this case, uses a prepackaged FEM. A forward model defines the finite element geometry, regions within the body (i.e. organs), electrode sizes and locations, and has pointers to approriate FEM forward solvers. Onto `fmdl`, the pattern of stimulation and measurement must be assigned (line 2); here using a function to define adjacent stimulation and measurement onto two rings of 16 electrodes. Next (line 3), an inverse model for difference EIT is defined (`select_imdl`), for which a reconstructed parameterization is created over a voxel volume (`mk_voxel_volume`). In line 4, options for the GREIT model are defined; here the noise performance and target radius are set, and other values left to the default. Last, in line 5, `mk_GREIT_model` is called to create the GREIT inverse model, `imdl`. EIDORS creates a 3D solver, based on the 3D voxel volume provided.

Listing 1: Example script to create a 3D GREIT inverse model.

```
1  fmdl = mk_library_model( 'cylinder_16x2el_coarse' );
2  fmdl.stimulation = mk_stim_patterns( 16, 2, [0,1], [0,1]);
3  imdl = mk_voxel_volume( select_imdl( fmdl ));
4  opt.noise_figure= 1.0; target_radius= 0.15;
5  imdl = mk_GREIT_model( imdl, target_radius, [], opt);
6  imgr = inv_solve(imdl, v_time0, v_time1);
```

In line 6, the inverse solver, `imdl` (created in the line 5), is used to reconstruct image `imgr`. Since this is a difference image, two measurements are required, `v_time0` and `v_time1`. This image can then be rendered in 3D or using various slice selection approaches. The preceeding example shows a use of the default parameters. The documentation for each function shows the use of optional values to adjust the algorithm.

References

Ackerman M J 1998 The Visible Human Project *Proc. IEEE* 86 504–511

Adler A and Lionheart W R B 2006 Uses and abuses of EIDORS: An extensible software base for EIT *Physiol Meas* 27 S25–S42

Adler *et al* GREIT 2009 Adler A Arnold JH Bayford R Borsic A Brown BH Dixon P Faes TJC Frerichs I Gagnon H Gärber Y Grychtol B Hahn G Lionheart WRB Malik A Patterson R Stocks J Tizzard A William R Wolf GK 2009 GREIT a unified approach to 2D linear EIT reconstruction of lung images *Physiol Meas* 30 S35–S55

Adler A and Lionheart WRB 2011 Minimizing EIT image artefacts from mesh variability in Finite Element Models *Physiol Meas*, 32 823–834

Adler A Gaggero PO and Maimaitijiang 2011 Adjacent Stimulation and Measurement Patterns Considered Harmful *Physiol Meas*, 32 731–744

Adler A Boyle A Crabb MG Gagnon H Grychtol B Lesparre N Lionheart WRB 2015a EIDORS Version 3.8 p 19, *Proc EIT2015*, Neuchâtel, Switzerland, Jun 2–5

Adler A Frerichs I Grychtol B 2015b "The off-plane sensitivity of EIT", p 68, *Proc EIT2015*, Neuchâtel, Switzerland, Jun 2–5

Ahn S Wi H Oh TI McEwan AL Jun SC Woo EJ 2014 Continuous Nondestructive Monitoring Method Using the Reconstructed Three-Dimensional Conductivity Images via GREIT for Tissue Engineering *J Applied Math* 562176

Ambrisko T Science J Adler A Kutasi O Makra Z Moens Y 2015 Assessment of distribution of ventilation by electrical impedance tomography in standing horses In press: *Physiol Meas*, Nov 2015

Borsic A Halter R Wan Y Hartov A and Paulsen KD 2010 Electrical impedance tomography reconstruction for three-dimensional imaging of the prostate. *Phys Meas* 31 S1–S16.

Bayford RH Kantartzis P Tizzard A Yerworth R Liatsis P and Demosthenous A 2008 Development of a neonate lung reconstruction algorithm using a wavelet AMG and estimated boundary form *Physiol Meas* 29 S125–S138

Blue RS Isaacson D and Newell JC 2000 Real-time three-dimensional electrical impedance imaging *Physiol Meas* 21 15–26

Gaggero PO Adler A and Grychtol B 2014 Using real data to train GREIT improves image quality p 39, *Proc EIT2014*, Gananoque, Canada, Apr 24–26

Graham B and Adler A 2007 Electrode Placement Configurations for 3D EIT *Physiol Meas*, 28 S29–S44

Grychtol B and Adler A 2014 Choice of reconstructed tissue properties affects interpretation of lung EIT images *Physiol Meas* 35 1035–1050

Grychtol B and Adler A 2013 FEM electrode refinement for Electrical Impedance Tomography *Conf IEEE Eng Med Biol Soc*, pp. 6429–6432, Osaka, Japan, July 3–7

Grychtol B Lionheart WRB Bodenstein M Wolf GK and Adler A 2012 Impact of model shape mismatch on reconstruction quality in Electrical Impedance Tomography *IEEE Trans Med Imag*, 31(9) 1754–1760

Knudsen K Lassas M Mueller JL and Siltanen S 2009 Regularized D-bar method for the inverse conductivity problem. *Inverse Problems and Imaging* 35 599–624

Metherall P, Barber DC, Smallwood RH, Brown BH "Three dimensional electrical impedance tomography", *Nature* 380:509-512, 1996.

Newell JC Blue RS Isaacson D Saulnier GJ Ross AS 2002 Phasic three-dimensional impedance imaging of cardiac activity *Physiol Meas* 23 203–209.

Putensen C, Zinserling J, Wrigge H "Electrical Impedance Tomography for Monitoring of Regional Ventilation in Critically III Patients", *Int Care Med* 448–457, 2006.

Rabbani KS and Kabir ABMH 1991 Studies on the effect of the third dimension on a two dimensional EIT system *Clin Phys Physiol Meas* 12: 393–402

Schöberl J, "NETGEN – An advancing front 2D/3D-mesh generator based on abstract rules." *Comput Visual Sci*, 1:41–52, 1997.

Petersen KB and Pedersen MS "The Matrix Cookbook, Version 20121115", *Technical University of Denmark*, 2012

Tizzard A Horesh L Yerworth R J Holder D S Bayford R H 2005 Generating accurate finite element meshes for the forward model of the human head in EIT *Physiol Meas* 26 S251–61

Vonk Noordegraaf A Faes TJC Janse A Marcus JT Heethaar RM Postmus PE and de Vries PMJM 1996 Improvement of cardiac imaging in electrical impedance tomography by means of a new electrode configuration. *Physiol Meas*, 17:179–188.